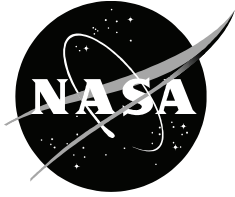# Rotor CFD Analysis at Terrestrial and Martian Atmospheric Densities

Brenda Natalia Perez Perez
Science and Technology Corporation
Moffett Field, California

September 2018

NASA STI Program ... in Profile

Since its founding, NASA has been dedicated to the advancement of aeronautics and space science. The NASA scientific and technical information (STI) program plays a key part in helping NASA maintain this important role.

The NASA STI program operates under the auspices of the Agency Chief Information Officer. It collects, organizes, provides for archiving, and disseminates NASA's STI. The NASA STI program provides access to the NTRS Registered and its public interface, the NASA Technical Reports Server, thus providing one of the largest collections of aeronautical and space science STI in the world. Results are published in both non-NASA channels and by NASA in the NASA STI Report Series, which includes the following report types:

- TECHNICAL PUBLICATION. Reports of completed research or a major significant phase of research that present the results of NASA Programs and include extensive data or theoretical analysis. Includes compilations of significant scientific and technical data and information deemed to be of continuing reference value. NASA counterpart of peer-reviewed formal professional papers but has less stringent limitations on manuscript length and extent of graphic presentations.

- TECHNICAL MEMORANDUM. Scientific and technical findings that are preliminary or of specialized interest, e.g., quick release reports, working papers, and bibliographies that contain minimal annotation. Does not contain extensive analysis.

- CONTRACTOR REPORT. Scientific and technical findings by NASA-sponsored contractors and grantees.

- CONFERENCE PUBLICATION. Collected papers from scientific and technical conferences, symposia, seminars, or other meetings sponsored or co-sponsored by NASA.

- SPECIAL PUBLICATION. Scientific, technical, or historical information from NASA programs, projects, and missions, often concerned with subjects having substantial public interest.

- TECHNICAL TRANSLATION. English-language translations of foreign scientific and technical material pertinent to NASA's mission.

Specialized services also include organizing and publishing research results, distributing specialized research announcements and feeds, providing information desk and personal search support, and enabling data exchange services.

For more information about the NASA STI program, see the following:

- Access the NASA STI program home page at http://www.sti.nasa.gov

- E-mail your question to help@sti.nasa.gov

- Phone the NASA STI Information Desk at 757-864-9658

- Write to:
  NASA STI Information Desk
  Mail Stop 148
  NASA Langley Research Center
  Hampton, VA 23681-2199
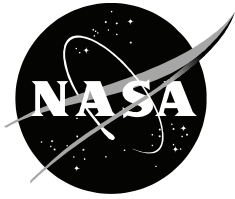
Rotor CFD Analysis at Terrestrial and Martian Atmospheric Densities

Brenda Natalia Perez Perez
Science and Technology Corporation
Moffett Field, California

National Aeronautics and
Space Administration

Ames Research Center
Moffett Field, CA 94035-1000

September 2018

Acknowledgments

I would like to express my utmost thanks and sincere gratitude to Dr. Warmbrodt for his mentorship and tremendous support.

My deepest gratitude to Witold Koning, without whose knowledge, support, and guidance this study would not have been possible. A special thanks to Geoffrey Ament for his assistance and contribution to the experimental data used in this project.

I would like to thank Michelle Dominguez, Marshall Yale, Dorsa Shirazi, and Colin Lauzon. Without their help, all the cases would not have been able to run in time. A special thanks to Hiram Cardona who was always extremely kind to me even when I asked to continuously review every single version of this project.

TABLE OF CONTENTS

LIST OF FIGURES

LIST OF TABLES

NOMENCLATURE

Abbreviations

ACT	Aerodynamic coefficients table
AWT	Aeolian Wind Tunnel
C81Gen	C81Generator
CFD	Computational fluid dynamics
CFL	Courant–Friedrichs–Lewy
FF	Free field
FFH	Free field hover
FFV	Free field with forward velocity
GRS	Grid Resolution Study
MDC	Martian density conditions
MG	Motor geometry
MH	Mars Helicopter
P1	Pressure at 20 mbar
P2	Pressure at 30 mbar
P3	Pressure at 42 mbar
PAV	Planetary Aerial Vehicle
P_{EXP}	Experimental power
P_{SIM}	Power in the simulation
RotCFD	Rotorcraft CFD
RotUNS	Rotorcraft Unstructured Flow Solver
S1	Original settings
S2	Change in settings
TDC	Terrestrial density conditions
T_{EXP}	Experimental thrust
T_{SIM}	Thrust in the simulation

Symbols

A_i	Area at the inlet of the wind tunnel
A_r	Area of the rotor
C_T	Thrust coefficient
M	Mach number
R	Rotor radius
Re	Reynolds number
T	Thrust
V	Velocity magnitude
v_h	Rotor induced velocity
V_{stream}	Velocity at the inlet of the wind tunnel

Greek

ΔT	Time step
ΔX	Length of the smallest cell
Ω	Rotational velocity
ρ	Density

Rotor CFD Analysis at Terrestrial and Martian Atmospheric Densities

Brenda Natalia Perez Perez[*]

Ames Research Center

SUMMARY

Much effort has been made to enhance exploration on Mars. In addition to a rover and Mars-orbiting satellites, a Mars Helicopter (MH) was proposed to augment planetary research. Computational fluid dynamics (CFD) simulations have been performed to increase the understanding of the behavior and performance of vertical lift Planetary Aerial Vehicles (PAVs). Because of the large difference in atmospheric conditions between Mars and Earth, predicting and testing rotorcraft performance is a complex task. The goal of this project was to understand the capability of the mid-fidelity CFD software RotCFD to predict the performance of a single rotor in terms of thrust and power at 1013.25 millibar and 14 millibar, which corresponds to terrestrial and Martian atmospheric densities, respectively. Also, in order to characterize wind tunnel wall effects, free field and wind tunnel simulations were performed, analyzed, and compared. Different analytical tools have been used to aid in the design process for the future vertical lift PAVs. One of them includes experimental tests performed on a rotor in the Aeolian Wind Tunnel (AWT) facility at NASA Ames Research Center under different pressure conditions ranging from terrestrial to Martian atmospheric conditions. C81Generator was also used in this research to capture the aerodynamic coefficients of the rotor airfoils based on the Mach number, Reynolds numbers, and angles of attack used in the experimental tests. The rotor model that resulted from this effort was input into RotCFD, and various simulations were performed under terrestrial and Martian density conditions in order to mimic the experimental test. Finally, the results from RotCFD were compared with the collected test data of the AWT.

INTRODUCTION

A rotor experiment was performed at NASA Ames Research Center in the Planetary Aeolian Laboratory. This building contains a test chamber that has the capability to parallel Martian atmospheric densities by pumping pressure down from 1 bar to 5.5 mbar.

The goal of this project was to perform CFD analyses of this single rotor experiment to understand the capability of the mid-fidelity CFD software RotCFD to predict rotor performance in terms of thrust and power at 1013.25 mbar and 14 mbar, which correspond to terrestrial and Martian atmospheric conditions, respectively. Moreover, this project characterized motor geometry and wind tunnel wall effects by simulating multiple cases with four different configurations: free field hover (FFH), free field with forward velocity (FFV), Aeolian Wind Tunnel (AWT), and AWT with motor geometry (MG).

Furthermore, efforts were made to analyze the effects of different factors in the simulation that may be contributing to the discrepancy of the results. These factors include the length of the wind tunnel, time of the simulation, cell density, velocity at the inlet of the wind tunnel, atmospheric pressure, and tables of aerodynamics coefficients used in RotCFD.

---

[*] Science and Technology Corporation, Moffett Field, CA.

Finally, this report contains an explanation of the approach followed, as well as the settings used in each of the simulations.

N242 EXPERIMENT DESCRIPTION

A single 1.02-m-diameter rotor was tested in forward flight. The rotor was mounted in the wind tunnel at −14 degrees angle of attack, where the wind tunnel cross-section height and width are 0.96 m and 1.22m, respectively (see Figure 1).

Data was collected at different pressures ranging from 1 atmosphere to 5.5 mbar. The results of the simulations were compared with the experimental data shown in Appendix A.

Figure 1. Single rotor at shaft angle of −14 degrees (ref. 1).

APPROACH

In order to obtain rotor performance data and understand the predictive capability of RotCFD (with the RotUNS solver) multiple simulations were performed at both 1013.25 mbar and 14 mbar. The wall and motor geometry effects were also analyzed during these wind tunnel simulations.

This section explains the four different cases that were modeled for this purpose: FFH, FFV, AWT with the isolated rotor, and AWT with MG. Furthermore, the change of some of the variables in the simulations, such as length of the wind tunnel, time of the simulation, free stream velocity, and grid density, are described. Similarly, the process used to obtain the aerodynamic coefficients needed for the RotCFD simulation is shown.

Figure 2 shows the approach followed in this research (ref. 2).

Airfoil sections were obtained from 3D scanned data of the rotor used in the Mars Rotor test.

XFOIL was used to optimize the number of panels in the airfoils to increase accuracy.

C81Generator was used to obtain aerodynamic coefficients of the airfoil sections based on the angle of attack and Mach number of the experimental test.

The tables of the **aerodynamic coefficients were post-processed** to identify possible outliers; the data was stitched for high angles of attack.

Multiple **simulations were run in RotCFD** using the previously obtained aerodynamic coefficients.

The **results** from both the **experimental data** and **simulations** were **compared.**

Figure 2. Diagram of the approach followed for this research.

SIMULATIONS

C81Generator

C81Generator (C81Gen) was used to obtain the lift, drag, and moment coefficients of the airfoil sections. The airfoil sections selected from the scanned data correspond to the blade radial position 21 percent, 29 percent, 74 percent, and 95 percent.

The tables of aerodynamic coefficients were obtained in C81Gen. The input in this software uses the expected temperature, angle of attack, Reynolds number, and Mach number of the experimental tests. Moreover, Koning, Johnson, and Allan performed a Grid Resolution Study (GRS) in C81Gen for the airfoil deck in their studies to generate a performance model for the Mars Helicopter rotor, which, as in this study, works under very low Reynolds Number ($Re_c = 10^3$ to $Re_c = 10^4$) (ref. 3). They found that by increasing the grid density beyond the settings shown in Table 1, the results exhibited changes in drag below 1 drag count. Thus, the grid settings shown in Table 1 were used in this project for the generation of the aerodynamic coefficient tables in C81Gen. The C81Gen grid is shown in Figure 3.

Table 1. Grid settings.

Streamwise points	501
Normal points	167
Wake points	83
y^+	0.5
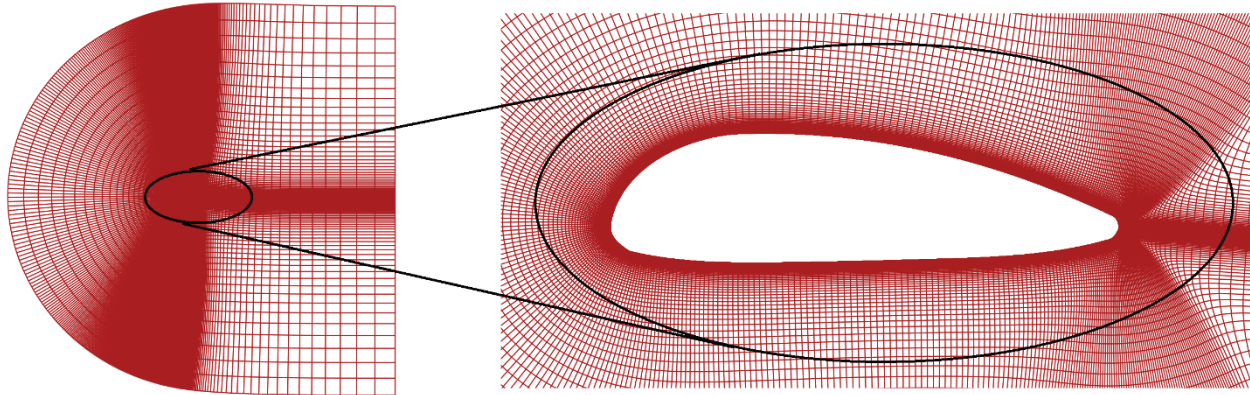
Figure 3. Close view of C81Gen grid.

Summary of the Simulations in RotCFD

This section shows the scope and description of the four different types of assessments and the variations used for the simulation. Table 2 is a summary of the simulations that were performed at 1013.25 mbar and 14 mbar.

Table 2. Different types of simulations.

	1013.25 mbar	14 mbar
Assessment 1—Free Field Hover (FFH)		
1. FFH	●	●
2. FF run at two lower tip speeds	●	●
Assessment 2—Free Field With Forward Velocity (FFV)		
1. FFV	●	●
2. FF run at two lower tip speeds	●	●
Assessment 3—Aeolian Wind Tunnel (AWT)		
1. Larger wind tunnel length and longer simulation time	●	●
2. Shorter wind tunnel length and simulation time	●	●
3. Shorter wind tunnel length and simulation time run at two lower tip speeds	●	●
4. Increase in free stream velocity in shorter wind tunnel length and simulation time	●	●
Assessment 4—AWT and Motor Geometry (MG)		
1. Shorter wind tunnel length and simulation time	●	●
2. Shorter wind tunnel length and simulation time run at two lower tip speeds	●	●
3. Increase in free stream velocity in shorter wind tunnel length and simulation time		●
Changes in Grid Density		
1. FFH configuration with roughly 60% less cells		●
2. MG configuration with more body refinement		●
3. AWT and MG configuration with roughly 60% less cells		●

Three different rotor tip speeds were used in each case to parallel the range of rotational speed used in the AWT experiment, which varied from approximately 2000 to 3000 RPM for 14 mbar, and 700 to 2180 RPM for 1013.25 mbar.

The pressures of 1013.25 mbar and 14 mbar were selected to roughly match the terrestrial density conditions (TDC) and Martian density conditions (MDC) (ref. 3), respectively.

To obtain a better understanding of how the thrust and power change with the variation of pressures, three more FFH cases were performed at 20 mbar (P1), 30 mbar (P2), and 42 mbar (P3). Table 3 shows the atmospheric conditions used in the RotCFD simulations.

Every case performed during this research used the steady state rotor model where the discrete rotor source terms are averaged over the disc (ref. 4).

Table 3. Atmospheric conditions.

Atmospheric Conditions	TDC	MDC	P1	P2	P3
Static Density (kg/m^3)	1.225	0.016	0.023	0.036	0.050
Static Temperature (K)	288.160	288.520	290.150	290.494	291.150
Gas Constant (m^2/s^2/K)	287	287	287	287	287
Specific Heat Ratio (~)	1.4	1.4	1.4	1.4	1.4
Dynamic Viscosity (Kg/ms)	1.750E-05	1.750E-05	1.750E-05	1.750E-05	1.750E-05
Static Pressure (Pa)	101,325	1,400	2,000	3,000	4,200

1013.25 mbar simulation

This research also sought to analyze and discard the possible factors that could be contributing to the difference in the simulation results compared to the experimental data shown in Appendix A. Hence, as there is more certainty and understanding on the measurements systems on a well-known condition, the four different assessments were run at terrestrial conditions. Therefore, the 1013.25 mbar simulation could be used as a "trusted reference point" to discard some of the same settings used for both Martian and terrestrial cases as error contributors. For instance, the scanned airfoil geometry of the rotor (used for both 14 mbar and 1013.25 mbar C81Gen simulations) could be validated if the results of the simulation correlate well with the experimental data at 1013.25 mbar. Moreover, the behavior of the changes within the cases was observed and compared for these two pressures.

Free Field Hover (FFH)

This case is an isolated rotor with no wind tunnel wall effects. A representation of the case is shown in Figures 4 through 6.

The corresponding atmospheric pressure of each simulation is used as a boundary condition on every side of the domain with the exception of the rotor wake region, which is configured to mass outflow.

The size of the domain was large enough to prevent being adversely influenced by the established boundary conditions and close enough to allow for greater cell density. The domain size and distribution of the cells have to be wisely chosen because the maximum number of cells is limited by the available graphics card memory (GPU RAM), which in this case was approximately 1.3 million cells.
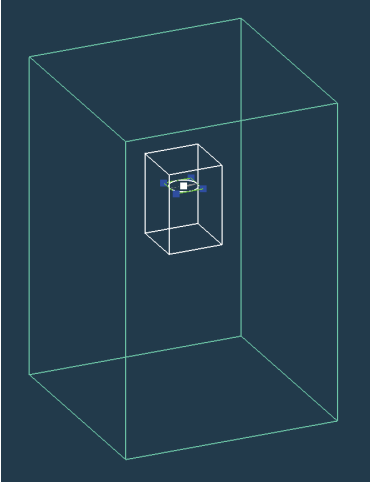
Figure 4. Free field assessment.
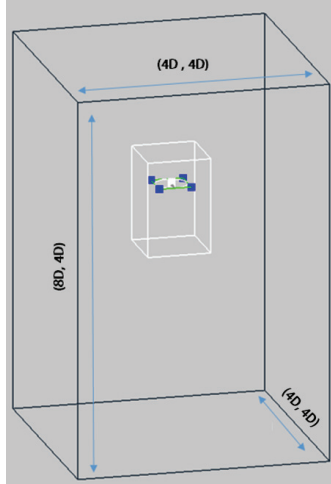
Figure 5. Dimensions of the boundary in terms of rotor diameters measuring from the center of the rotor.
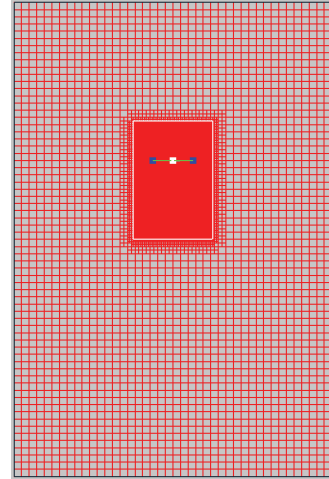
Figure 6. Grid of free field configuration.

Grid specifications

The selection of the grid settings was determined by the following criteria:

1. Obtain square grids.
2. Increase cell density near the rotor.
3. Minimize abrupt changes on grid size within the boundary.
4. Keep the cell count lower than 1.3 million.

Tables 4 and 5 summarize the configurations used in the grid specification section.

Table 4. Grid specifications.

Boundary X Cells	42
Boundary Y Cells	42
Boundary Z Cells	63
Gen. Rotor Refinement	4
Rotor Box Size	1.1
Number of Cells	1,153,579

Table 5. Refinement box settings.

	X (m)	−1
Lower Corner	Y (m)	−1
	Z (m)	−2
	X (m)	1
Upper Corner	Y (m)	1
	Z (m)	1
Refinement	4	

Time grid

To attain case convergence, the time length and time steps were set to 25 revolutions of the rotor, and 1 degree of rotation per time step.

To achieve 25 revolutions in the simulation at an angular velocity of 3000 RPM (or 50 revolutions per second) the time length of the simulation would have to be 0.5 second. Similarly, in order to observe 1 degree of rotation each time step, 360 time steps are necessary for 1 revolution. Hence, as 25 rotations were desired, 9,000 time steps were used. Table 6 shows a summary of the time length and time steps used for three different tip speeds.

Table 6. Sample table of RPM, time length, and time steps used at reduced pressures.

RPM	Time Length (s)	Time Steps
2,000	0.75	9,000
2,500	0.60	9,000
3,000	0.50	9,000

Free Field With Forward Velocity (FFV)

This assessment used the same configuration as the FFH with the exception of the boundaries, which were set to experience a forward velocity with a rotor angle of attack of −14 degrees. A better approach to simulate this type of case in RotCFD is to modify the velocity vector instead of rotating the object (ref. 5).

The forward velocities in this FFV assessment match the wind tunnel inlet velocities of the AWT assessment shown in Table 7. Figure 7 is a representation of the velocity vectors used in the boundaries; for the case where the flow is traveling at 5 m/s, the "x" component is set to 0, "y" is set to 4.8514 m/s, and "z" is set to −1.2096 m/s.
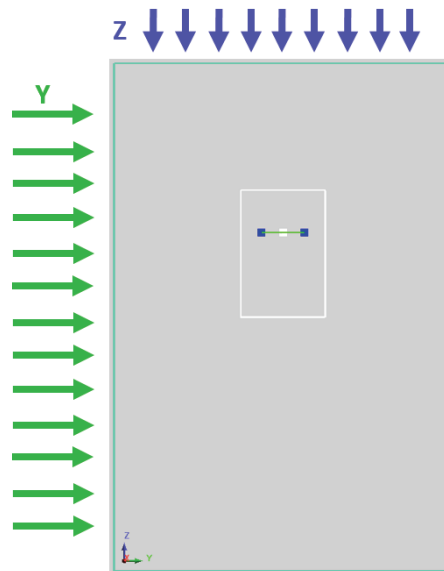
Figure 7. Representation of the velocity vectors in the boundaries.

Aeolian Wind Tunnel (AWT)—Long Wind Tunnel Length

The streamwise length of the tunnel case was set long enough to observe the full development of the rotor wake. The longest wake development was expected to be seen at the highest tip speed, therefore this simulation was only run for the maximum tip speed analyzed at 1 atmosphere and 14 mbar. Once this case was solved and the flow was observed, the length was shortened at a relevant point. The same case was run again for both pressure conditions but this time with the shorter length to verify that the change in length did not change the results.

Boundaries

The cross section of the boundary and refinement box was defined by the geometry of the wind tunnel. The length of the tunnel was set to 5 rotor diameters to the front and 10 rotor diameters to the back, measuring from the center of the propeller. The refinement box was set to 4 rotor diameters to the back and 2 rotor diameters to the front. A representation of the case is shown in Figure 8.
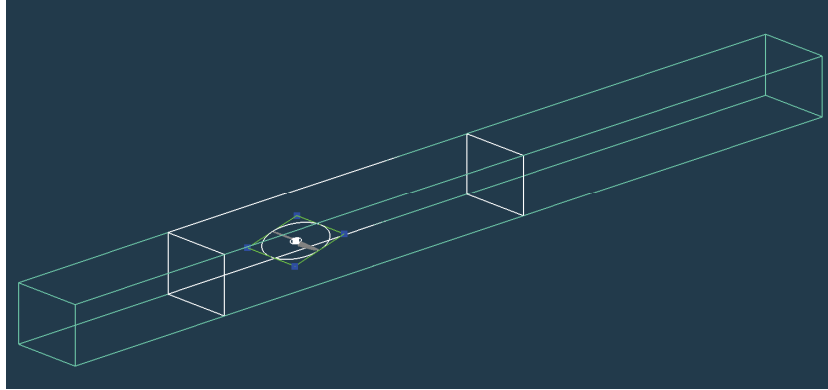
Figure 8. Long-length case of AWT.

The boundaries were set to viscous walls with the exception of front and back. The far end of the streamwise direction uses mass outflow correction, and the boundary condition at the inlet was set to free stream velocity.

The free stream velocity was approximated by using the momentum theory formula of the induced velocity of the rotor in hover (ref. 6), and the conservation of mass.

$$V_h = \left(\frac{T}{2\rho A_r}\right)^{\frac{1}{2}} \qquad V_{stream} = V_h\left(\frac{A_r}{A_i}\right)$$

Where,

V_h is the induced velocity of the rotor,

V_{stream} is the velocity at the inlet of the wind tunnel,

T is the experimental thrust at a certain pressure and tip speed,

ρ is the experimental density at a certain pressure,

A_r is the rotor disk area, and

A_i is the area at the inlet of the wind tunnel.

Table 7 summarizes the free stream velocities used.

Table 7. Inlet velocities.

1 Atmosphere		14 mbar	
RPM	Inlet Velocity (m/s)	RPM	Inlet Velocity (m/s)
2,180	6.64	3,000	7.30
1,500	5.00	2,500	5.00
700	2.00	2,000	5.00

Grid specifications

The selection of the grid settings was determined by the following criteria:

1. Obtain square grids.
2. Increase cell density near the rotor.
3. Have enough refinement on the walls.
4. Keep the cell number lower than 1.3 million.

Tables 8 and 9 summarize the configurations used in the grid specification section. Figure 9 shows the grid of the AWT long-length configuration.

<div style="display:flex">

Table 8. Grid specifications.

Boundary X Cells	14.0
Boundary Y Cells	172.0
Boundary Z Cells	11.0
Gen. Rotor Refinement	3.0
Rotor Box Size	1.1
Number of Cells	900,032.0

Table 9. Refinement box settings.

Lower Corner	X (m)	−0.6096
	Y (m)	−2.0000
	Z (m)	−0.4826
Upper Corner	X (m)	0.6096
	Y (m)	4.0000
	Z (m)	0.4826
Refinement		3.0000

</div>
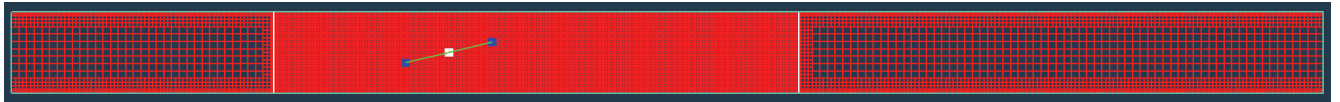
Figure 9. Grid of the AWT long-length configuration.

Time grid

The time was selected to allow one particle to travel twice the streamwise length. Moreover, this same simulation was done with twice the time to ensure that the time did not affect the results and that there was no more development in the wake.

The time steps were selected by obtaining a CFL number smaller than 1 (it was desired that the fluid particles would move only from one cell to its immediate neighbor within one time step).

$$CFL = \frac{V * \Delta T}{\Delta X}$$

Where,

V is the velocity magnitude,

ΔT is the time step, and

ΔX is the length of the smallest cell.

Although the flow does not move as fast as the tip speed of the rotor, this was used as the velocity in the CFL formula to ensure that the velocity of the flow was fully covered for the wind tunnel cases.

Appendix B shows a summary of the number of time steps used in these simulations.

Aeolian Wind Tunnel (AWT)—Short Length

Boundaries

This configuration (see Figure 10) used the same boundaries as the previous configuration with the exception that 4 rotor diameters were used in the streamwise direction instead of 10. This reduction in length decreased the time of the simulation from 130 hours to 33 hours.

All the decisions for the settings were made with the same considerations as those explained in the AWT long-length assessment.

Tables 10 and 11 summarize the configurations used in the grid specification section.
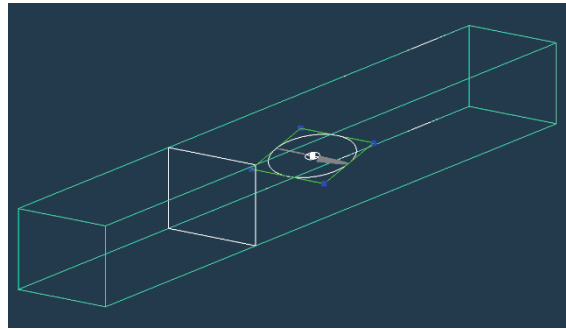
Figure 10. Short-length case of AWT.

<table>
<tr><td colspan="2" align="center">**Table 10. Grid specifications.**</td></tr>
<tr><td>Boundary X Cells</td><td>16</td></tr>
<tr><td>Boundary Y Cells</td><td>118</td></tr>
<tr><td>Boundary Z Cells</td><td>13</td></tr>
<tr><td>Gen. Rotor Refinement</td><td>3</td></tr>
<tr><td>Rotor Box Size</td><td>1.1</td></tr>
<tr><td>Number of Cells</td><td>1,148,968</td></tr>
</table>

Table 11. Refinement box settings.

Lower Corner	X (m)	–0.6096
	Y (m)	–2.0000
	Z (m)	–0.4826
Upper Corner	X (m)	0.6096
	Y (m)	4.0000
	Z (m)	0.4826
Refinement		3

Aeolian Wind Tunnel (AWT) and Motor Geometry (MG)

This configuration also followed the same process for the settings as those explained in the AWT long-length section, and it used the same boundaries as the short-length case. In contrast to the assessments where the wind tunnel was modeled, this case sought to analyze the effects of the flow interference due to the geometry below the rotor. A simplified version of the motor as shown in Figure 11 was modeled to investigate how the interference of the flow with the motor contour would affect the rotor performance. A 3D model of the rotor was inserted into the wind tunnel at –14 degrees. Figures 12 and 13 show the AWT and MG configuration.

10
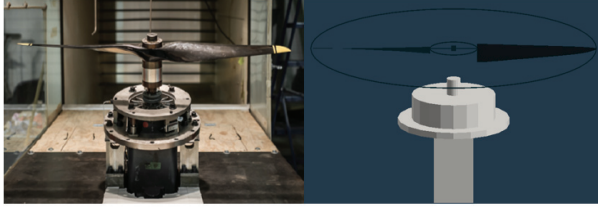
Figure 11. Real geometry of the motor vs. idealized geometry.
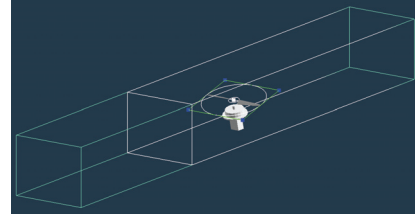
Figure 12. AWT case including the MG.
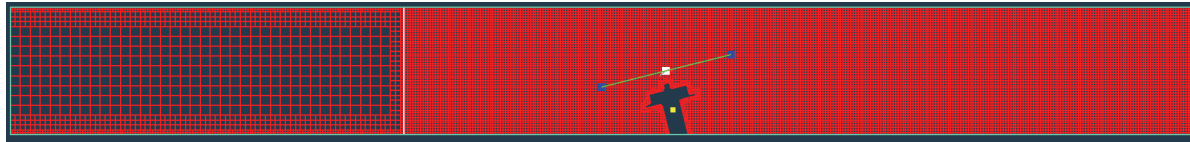
Figure 13. AWT and MG grid.

Grid specifications

Tables 12 and 13 summarize the configurations used in the grid specification section. This assessment used the same values for the refinement box as those used for the AWT short-length case.

Another aspect that was analyzed was the increase in the body refinement. As shown in Table 12, the number of cells is nearly at the 1.3 million cell limit. In fact, to run another simulation with increased refinement of the cells near the body, the boundary grid density had to be decreased. Figures 14 and 15 show the difference in body refinement within these cases. This simulation was only run at 3,000 RPM to compare with the coarse refinement near the body simulation at the same tip speed.

Table 12. Grid specifications.

Boundary X Cells	16
Boundary Y Cells	118
Boundary Z Cells	13
Gen. Rotor Refinement	3
Rotor Box Size	1.1
Gen. Body Refinement	3
Number of Cells	1,163,743

Table 13. Grid specifications with increase in body refinement.

Boundary X Cells	14
Boundary Y Cells	103
Boundary Z Cells	11
Gen. Rotor Refinement	3
Rotor Box Size	1.1
Gen. Body Refinement	4
Number of Cells	816,593
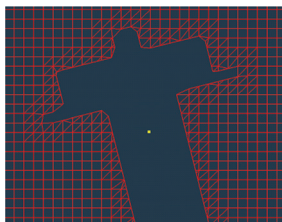
Figure 14. Grid cells with body refinement of 3.
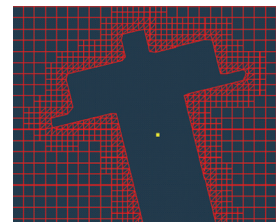
Figure 15. Grid cells with body refinement of 4.

RESULTS

Continuum-type Flow in the Experiment

The ranges in Mach and Reynolds numbers exhibited during the reduced pressure experiment were observed to understand more about the expected behavior of the flow at such low densities and to determine if the flow can still be considered a continuum flow.

Table 14 shows the range of the Mach and Reynolds numbers corresponding to the tip speeds from 2,000 RPM to 3,000 RPM at 14 mbar. According to Hoerner (ref. 7), the flow within this range is still expected to behave as a continuum-type flow.

Table 14. Range of Mach and Reynolds numbers.

M	Re
0.0640 to 0.4470	1770.3 to 4566.6

Thrust and Power vs. Tip Speed

To have a better understanding of the expected behavior for the rotor performance in terms of thrust, power, and tip speed, the following equations were derived from the formula that describes the rotor thrust coefficient and power coefficient (ref. 6).

$$T = C_T \left[\rho A_r (\Omega R)^2\right] \qquad\qquad P = C_P \left[\rho A_r (\Omega R)^3\right]$$

Where,

- T: Rotor thrust
- P: Power
- C_T: Thrust coefficient
- C_P: Power coefficient

- ρ: Density
- A_r: Rotor disk area
- Ω: Tip speed
- R: Rotor radius

If the only variable is the angular velocity, and the thrust coefficient is behaving in its linear range, then the thrust is expected to increase linearly with the increase of RPM^2. Similarly, the power is expected to change in the same fashion with the increase of RPM^3. In fact, a linear regression was implemented to all the cases and experimental data to observe the correlation with this behavior.

At the time of the simulations, the specific experimental points that were to be used for comparison were unknown. Therefore, the three speeds used in the simulation covered the known range of RPM used in the experiment. Then, a linear regression was used to find the prediction of the simulation values at the same points where the experiment was analyzed. All of the assessments showed that the values were very close to the fitted line (R^2 very close to 1), as R^2 in all the cases was larger than 0.99.

Appendix C shows the equations of thrust and power obtained from the linear regression.

Rotor Performance for the Four Assessments

The following section shows rotor performance plots in terms of thrust vs. RPM^2 and power vs. thrust for both the terrestrial and Martian density conditions. The plots shown in Figures 16 through 19 compare the experimental data with the four simulation assessments.

<u>Thrust vs. RPM^2</u>
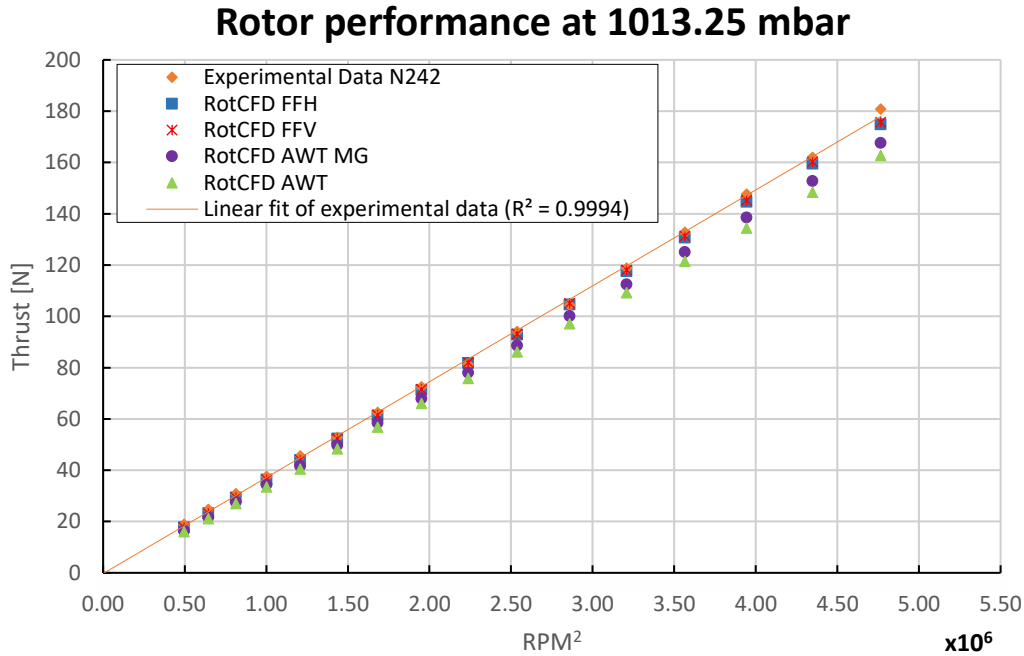
Figure 16. Thrust vs. tip speed at 1 atmosphere.

Figure 17. Thrust vs. tip speed at reduced pressure.

Rotor performance at 1013.25 mbar
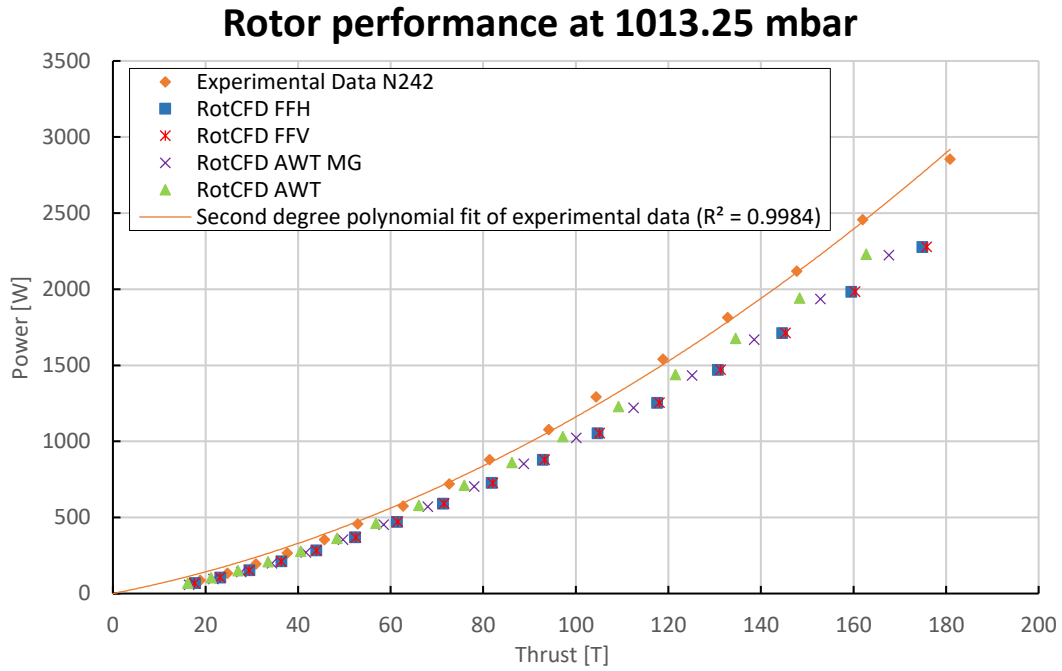
Figure 18. Power vs. thrust at 1 atmosphere.

Rotor performance at 14 mbar
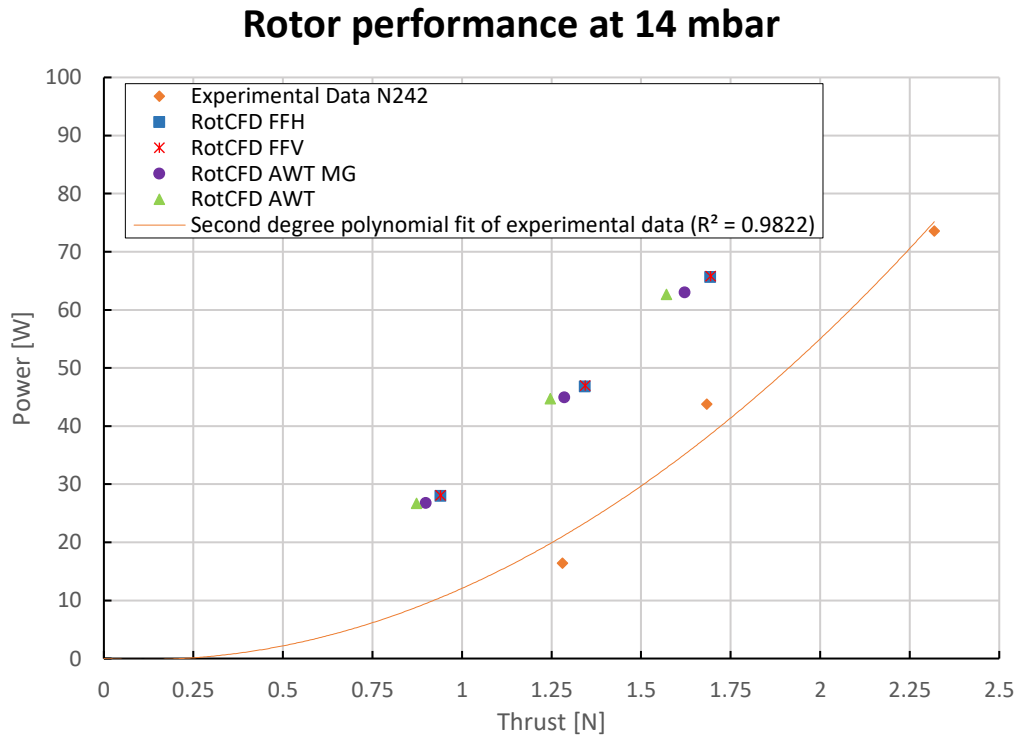
Figure 19. Power vs. thrust at reduced pressure.

The simulated thrust in the assessments compared to the experimental thrust reduces by around 26 percent and 5.5 percent for 14 mbar and 1013.25 mbar, respectively.
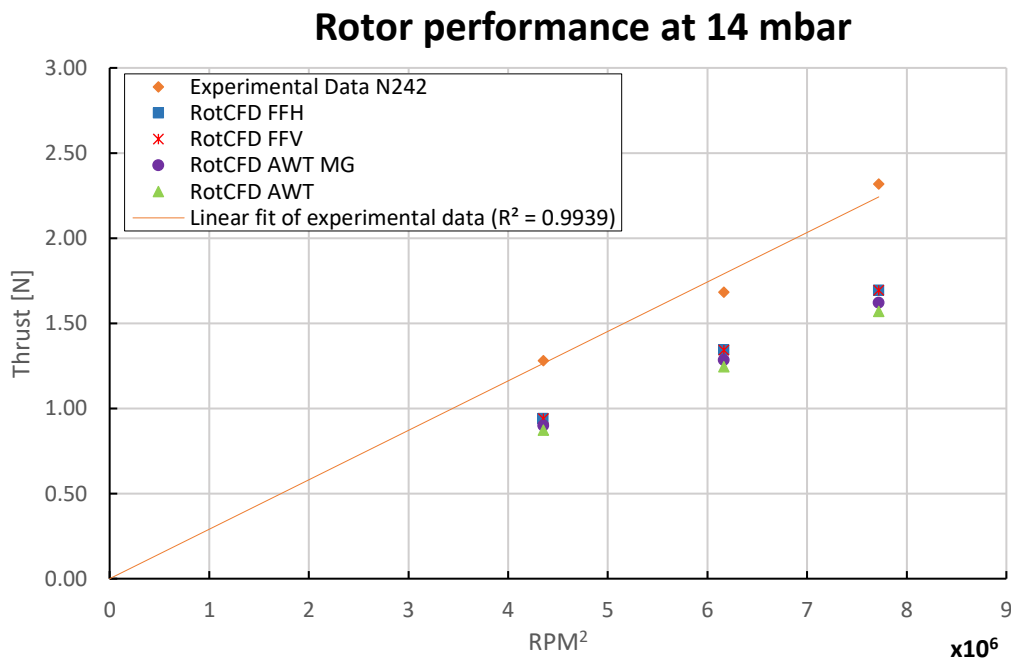
Although there is less overall thrust difference between measured and simulated thrust at reduced pressure, note that even a change of 1 Newton (N) can lead to a significant error because the magnitude of the thrust is very low at this reduced pressure. Conversely, a change of 1 N in thrust values in Earth simulations results in no significant difference in the percent error.

Further, the trend at 1 atmosphere shows that the percent error between the simulated and experimental thrust increases as the magnitude of the thrust decreases, while the power percent error remains roughly constant through the sweep of tip speeds. Table 15 shows the error percentage between the experimental and simulated values compared to the AWT assessment at 1 atmosphere.

Table 15. Error of the AWT assessment compared to the experimental values at 1 atmosphere.

RPM	AWT Thrust Error (%)	AWT Power Error (%)
705	14.59	21.88
1099	11.17	21.50
1397	9.00	19.52
2085	8.40	20.93

Perhaps one of the contributions to the greater error at reduced pressures is not a matter of differences between terrestrial and Martian conditions but the capacity or "resolution" of the experimental procedures and simulations to read and predict low values of thrust (even at terrestrial conditions).

The change in thrust needed to better approximate to the experimental results at reduced pressure is less than 0.8 N. Likewise, a change in power of roughly 10 W would be needed to obtain a closer experimental power. Therefore, efforts were made in the following sections to analyze multiple factors in the simulation to understand how the sensitivity of thrust and power results in these changes.

Analysis of the Geometry at 1 Atmosphere and Reduced Pressure

Thrust comparison of both atmospheric conditions at approximately the same tip speed

The experimental thrust at the RPM shown in Table 16 at 14 mbar and 1013.25 mbar are 1.28 N and 161.98 N, respectively.

Tables 16 through 19 compare the thrust and power between the results of the experiment and simulations of the four different assessments for both 14 mbar and 1013.25 mbar (1 atmosphere) at roughly the same tip speed.

The third column (Change (%)) in Table 16 shows the percent change between the experimental thrust and the simulated thrust at the corresponding assessment. The third column (Difference (%)) in Table 18 shows the percent difference between the experimental power and the simulated power at the corresponding assessment.

Tables 17 and 19 show the difference in percent change between the FFH and the other three assessments.

Table 16. Thrust comparison of the four assessments for both pressure conditions.

Assessment	14 mbar @2085 RPM			1013.25 mbar @ 2085 RPM		
	Thrust (N)	T_{EXP}-T_{SIM} (N)	Change (%)	Thrust (N)	T_{EXP}-T_{SIM} (N)	Change (%)
FFH	0.940	0.340	26.562	159.527	2.460	1.518
FFV	0.941	0.339	26.264	160.304	1.683	1.038
MG AWT	0.899	0.381	29.765	152.867	9.120	5.630
AWT	0.873	0.407	31.796	148.385	13.602	8.397

Table 17. Change in percent difference of assessments FFV, MG AWT, and AWT compared to FFH.

Change in Percent Difference Within Assessments	14 mbar	1013.25 mbar
FFH-FFV (%)	0.30	0.48
FFH-MG AWT (%)	3.20	4.11
FFH-AWT (%)	5.23	6.88

For both terrestrial and Martian conditions, the FFH and FFV assessments exhibit closer thrust values compared to the experimental data. Also, the increase in the difference between FFH and the other assessments (Table 17) is approximately consistent. In other words, the addition of walls and motor geometry to the simulation seems to have the same effect on the rotor thrust at reduced pressures and at 1 atmosphere. Thus, the difference in the geometry does not appear to be the main source of difference at reduced pressure between the experimental data and the simulations.

Power comparison of both atmospheric conditions at roughly the same tip speed

The experimental power at the RPM shown in Table 18 at 14 mbar and 1013.25 mbar is 16.43 W and 2456.99 W, respectively.

Table 18. Power comparison of the four assessments for both pressure conditions.

Assessment	14 mbar @2087 RPM			1013.25 mbar @ 2085 RPM		
	Power (W)	P_{EXP}-P_{SIM} (W)	Difference (%)	Power (W)	P_{EXP}-P_{SIM} (W)	Difference (%)
FFH	27.991	−11.557	70.327	1982.797	474.195	19.300
FFV	28.090	−11.657	70.931	1985.676	471.316	19.183
MG AWT	26.799	−10.365	63.074	1936.110	520.882	21.200
AWT	26.728	−10.295	62.643	1942.834	514.158	20.926

Table 19. Change in percent difference of assessments FFV, MG AWT, and AWT compared to FFH.

Change in Percent Difference Within Assessments	14 mbar	1 atm
FFH-FFV (%)	0.60	0.12
FFH-MG AWT (%)	−7.25	1.90
FFH-AWT (%)	−7.68	1.63

The power does not seem to be following a comparable trend as it was in the thrust tables between 1 atmosphere and 14 mbar for the four assessments. As opposed to the 14 mbar cases, the FFH and FFV at 1013.25 mbar assessments exhibit a closer power value to the experimental power. The effects of the walls cause a decrease in power for both atmospheric conditions.

Analysis on the AWT and AWT with MG Assessment

A summary of the analyzed factors at 14 mbar and 3000 RPM is shown in Tables 20 and 21.

Analysis made in the AWT case

The time of the simulation was doubled from 4.2 sec to 8.4 sec, and the length of the tunnel was increased from 5 rotor diameters to 10 rotor diameters measuring from the center of the rotor to the end of the wind tunnel in the streamwise direction. Moreover, the velocity at the inlet was increased to 9 m/s and 20 m/s.

To observe the effects of the cells reduction in the results of the simulation, the cell number was decreased about 60 percent from 1,163,743 to 763,114.

Table 20. Change in settings in AWT assessment.*

Settings Changed	Original Settings (S1)	Settings Changed (S2)
Velocity at the inlet of the wind tunnel	7.3 m/s	9.0 m/s and 20.0 m/s
Wind tunnel length (measured from center point of the rotor) and simulation time	5 D inlet direction and 4 D streamwise direction	5 D inlet direction and 10 D streamwise direction
	4.2 sec	8.4 sec
Cell density	1,148,968	751,478

*D denotes rotor diameters.

Analysis made in AWT with MG assessment

Because the AWT and AWT with MG assessments share the same configurations (with the exception of the body refinement), it was deemed unnecessary to run the same wind tunnel length and time increase analysis as the one performed for the AWT.

Therefore, for the AWT with MG case, the velocity at the inlet was increased from 7.3 m/s to 9 m/s. Next, the body refinement was increased from 3 to 4, and the same reduction in cells made in AWT was performed for the MG where the cell number was decreased by approximately 60 percent.

Table 21. Change in settings in AWT with MG assessment.

Settings Changed	Original Settings (S1)	Settings Changed (S2)
Velocity at the inlet of the wind tunnel	7.3 m/s	9.0 m/s
Body refinement	3.0	4.0
Cell density	1,163,743	763,114

Results

Tables 22 and 23 show the values of thrust after the corresponding change in settings (S2). The third column (Change from S1 to S2 (%)) shows the percentage change of the thrust between the original simulation (S1) and S2.

Table 22. Comparison between original simulations and simulations after the change in settings in AWT assessment.

Change in Settings in AWT Assessment	Thrust			Power		
	S1 (N)	S2 (N)	Change from S1 to S2 (%)	S1 (W)	S2 (W)	Change from S1 to S2 (%)
7.3 m/s to 9 m/s	1.84	1.90	3.43	78.82	80.01	1.51
7.3 m/s to 20 m/s	1.84	2.03	10.61	78.82	82.9	5.18
Change in wind tunnel length and time	1.84	1.84	0.00	78.82	78.94	0.15
Change in cell density	1.84	1.83	0.22	78.82	78.74	0.10

Table 23. Comparison between original simulations and simulations after the change in settings in AWT with MG assessment.

Change in Settings in AWT With MG Assessment	Thrust			Power		
	S1 (N)	S2 (N)	Change from S1 to S2 (%)	S1 (W)	S2 (W)	Change from S1 to S2 (%)
7.3 m/s to 9 m/s	1.91	1.94	1.57	79.45	80.66	1.52
Body refinement from 3 to 4	1.94	1.94	0.00	80.66	80.86	0.25
Change in cell density	1.91	1.91	0.00	79.45	79.55	0.13

The increase in velocity caused the greatest increase in thrust and power. Although 20 m/s may be much higher than the actual experimental velocity, this study was made to investigate how sensitive thrust and power are to the increase in wind tunnel velocity.

Even though these presented factors changed the thrust and power of the simulation, they did not seem to be the main contributors to the difference in the results.

Table 24 depicts a similar analysis made for the AWT assessment at 1013.25 mbar and 2180 RPM, showing as well that there is not a significant difference due to these factors presented in the table below. Likewise, the change in thrust shows similar sensitivity as the reduced pressure case because of the increase on the inlet velocity.

Table 24. Comparison between original simulations and simulations after the change in settings at 1 atmosphere for the AWT assessment.

Change in Settings in AWT Assessment	Thrust			Power		
	S1 (N)	S2 (N)	Change from S1 to S2 (%)	S1 (W)	S2 (W)	Change from S1 to S2 (%)
Change in wind tunnel length and time	162.49	163.59	0.68	2222.28	2209.29	0.58
6.64 m/s to 20 m/s	162.49	185.16	13.95	2222.28	2248.95	1.20

FFH assessment at reduced pressure

The cell number was decreased by approximately 60 percent. In Table 25, "S1" is the original simulation, which contains 1,153,579 cells, while "S2" contains 720,375 cells.

Table 25. Comparison of thrust between original simulations and simulations after the decrease in number of cells.

Change in Settings in FFH Assessment	Thrust			Power		
	S1 (N)	S2 (N)	Change from S1 to S2 (%)	S1 (W)	S2 (W)	Change from S1 to S2 (%)
Cell density	1.981	1.997	0.808	82.469	82.792	0.392

The thrust does not significantly change even at the reduced cell number. Note that all of the FF simulations performed used 1,153,579 cells. According to this analysis, the difference between the simulated and measured thrust values cannot be attributed to the number of cells.

Sensitivity to Pressure in RotCFD

Additional simulations at 20 mbar, 30 mbar, and 42 mbar were run with the FFH assessment to better understand how pressure affects the rotor thrust and power in the simulation. Figure 20 shows the thrust and power obtained in the simulations for three different tip speeds at the above mentioned pressures, and 14 mbar. Figure 20 also shows that for each of the 3 tip speeds, the thrust and power change proportionally with the change in pressure.

It was observed that for both cases of 14 mbar and 30 mbar, the thrust in the simulation was roughly 30 percent less than the experimental thrust. Note that at 14 mbar an inaccuracy of 4 mbar in the pressure measurements systems would lead to an error of 30 percent in the simulation.
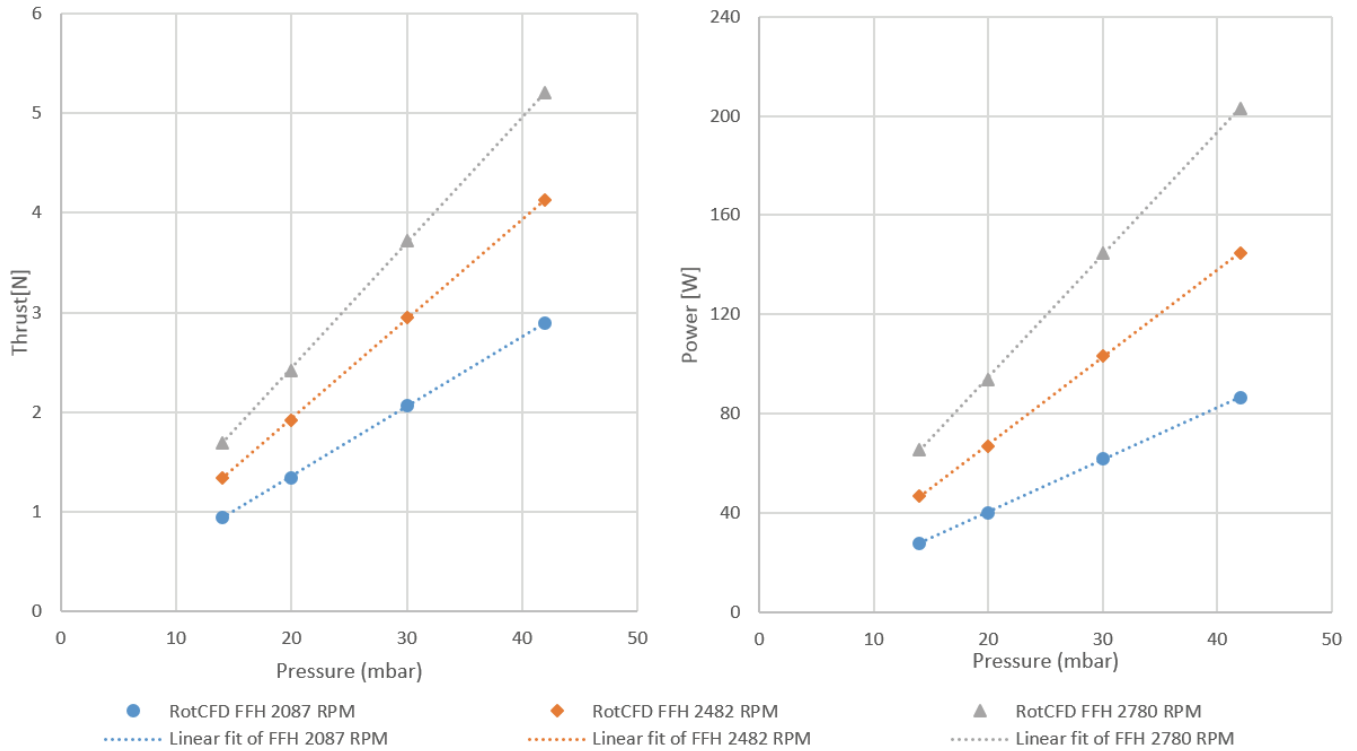
Figure 20. Thrust and power at different pressures and tip speeds.

Sensitivity of the Aerodynamic Coefficients to the Change of Pressure

To better understand how much the thrust could change with a change in aerodynamic coefficient table, an analysis was conducted to investigate how much the thrust and power changed by using 7 mbar tables for a 14 mbar simulation in RotCFD (see Table 26). The C81 aerodynamic coefficients table (ACT) corresponding to 7 mbar was provided by Koning (ref. 2).

When a 7 mbar airfoil table was used in the 14 mbar RotCFD simulation, the thrust was reduced by around 3.5 percent and the power was reduced by less than 1 percent.

Table 26. Thrust obtained at 14 mbar in RotCFD with a different set of ACT.

ACT	Thrust (N)	Power (W)
7 mbar	1.89	78.89
14 mbar	1.96	79.45

CONCLUSIONS

Geometry in the Simulation

The thrust and power for FFH and FFV exhibit very similar values. Compared to the free field assessments, the thrust decreases by roughly 4.5 percent for the AWT with MG, and 7.8 percent for the AWT with isolated rotor. Also, the AWT and AWT with MG exhibit similar values of power. The power decreases by around 5 percent when considering the geometry of the wind tunnel in the simulation.

The addition of walls and motor geometry in the simulation seem to have the same effect on the rotor thrust at reduced pressures and at 1 atmosphere. Thus, it appears that the highest error between the experimental data and simulations at reduced pressure does not lie within the geometry.

Resolution in Simulations and Experiments

The trend at 1 atmosphere shows that the error percentage between the simulated and experimental thrust increases as the magnitude of the thrust decreases. Future assessments could be done at 1 atmosphere to understand the capacity of the experimental procedures and simulations to read and predict low values of thrust similar to those seen at reduced pressures.

Effects on Rotor Performance Due to Change in Settings for the AWT and AWT With MG Assessments

The increase in length of the wind tunnel, time, and grid density in the simulation do not result in a meaningful change in thrust or power; the power and thrust appear to be more sensitive to the change in the velocity of the wind tunnel inlet. However, even if the wind tunnel inlet speed is changed in the simulation by 80 percent, the simulated thrust and power exhibit a change of no more than 10 percent.

Sensitivity to Pressure

The thrust and power in the simulations change proportionally with the change in pressure. An increase of 30 percent in the simulated thrust at reduced pressures exhibits closer values to the experimental thrust. Note that at 14 mbar, an experimental pressure transducer inaccuracy of 4 mbar leads to an error of about 30 percent when compared to the simulation.

Aerodynamic Coefficients

When a 7 mbar airfoil table is used in the 14 mbar RotCFD simulation, the thrust reduces by around 3.5 percent and the power reduces by less than 1 percent.

REFERENCES

1. G. A. Ament and W. J. F. Koning, "Isolated Rotor Forward Flight Testing From One Atmosphere Down to Martian Atmospheric Densities," American Helicopter Society Conference, Aeromechanics Design for Transformative Vertical Flight, San Francisco, CA, July 16-19, 2018.

2. W. J. F. Koning, "Generation of Performance Model for the Aeolian Wind Tunnel (AWT) Rotor at Reduced Pressure," NASA/CR-2018-219737, June 2018.

3. W. J. F. Koning, W. Johnson, and B. G. Allan, "Generation of Mars Helicopter Rotor Model for Comprehensive Analyses," American Helicopter Society Conference, Aeromechanics Design for Transformative Vertical Flight, San Francisco, CA, July 16-19, 2018.

4. W. J. F. Koning, "Wind Tunnel Interference Effects on Tilt Rotor Testing Using Computational Fluid Dynamics," NASA/CR-2016-219086, March 2016.

5. Surka Helitek, Inc., "How-To Guide: RotCFD version 0.9.15 (Beta)," Ames, IA, 2011.

6. W. Johnson, *Rotorcraft Aeromechanics*, New York, NY: Cambridge University Press, 2013.

7. S. F. Hoerner, *Fluid-Dynamic Drag: Practical Information on Aerodynamic Drag and Hydrodynamic Resistance*, ISBN-13: 978-9991194448, 1965.

APPENDIX A—Experimental Data

Table A.1. Experimental thrust for 14 mbar at different RPM.

14 mbar—Run 86				
Seq.	RPM	Thrust (N)	Power (W)	Advance Ratio
13	2086	1.280	16.434	0.080
12	2483	1.684	43.784	0.084
11	2778	2.319	73.569	0.085

Table A.2. Experimental thrust for 28 mbar at different RPM.

28 mbar—Run 87				
Seq.	RPM	Thrust (N)	Power (W)	Advance Ratio
23	2087	2.724	68.155	0.054
22	2481	4.969	127.985	0.059
21	2778	3.942	178.261	0.058

Table A.3. Experimental thrust for 1013.25 mbar at different RPM.

1013.25 mbar—Run 81				
Seq.	RPM	Thrust (N)	Power (W)	Advance Ratio
7	705	18.884	87.999	0.038
8	804	24.759	133.946	0.039
9	903	30.901	195.810	0.040
10	1002	37.641	266.815	0.040
11	1100	45.651	355.393	0.041
12	1199	52.907	458.386	0.041
13	1297	62.659	575.487	0.042
14	1397	72.639	720.565	0.041
15	1496	81.333	879.994	0.040
16	1593	94.177	1078.442	0.041
17	1691	104.389	1292.218	0.042
18	1791	118.843	1540.380	0.043
19	1888	132.828	1814.930	0.043
20	1986	147.730	2120.310	0.043
21	2085	161.987	2456.992	0.042
22	2183	180.866	2854.580	0.042

APPENDIX B—Time Steps

Table B.1. Time steps used at 14 mbar.

14 mbar	
Case	**Time Steps**
AWT Long—3000 RPM	36000
AWT Short	
3000 RPM	21000
2500 RPM	13800
2000 RPM	13400
MG	
3000 RPM	13800
2500 RPM	13800
2000 RPM	13800
Increased refinement—3000 RPM	31000

Table B.2. Time steps used at 1 atmosphere.

1 Atmosphere	
Case	**Time Steps**
AWT Long—2180 RPM	30000
AWT Short	
2180 RPM	12500
1500 RPM	7500
700 RPM	8500
MG 2180 RPM	11000

APPENDIX C—Equations of Thrust and Power

Table C.1. Equations of thrust and power in terms of tip speed for 1 atmosphere.

	Thrust (N)	Power (W)
FFH	$T = 3.6804E\text{-}05*RPM^2 - 0.5341$	$P = 2.1953E\text{-}07*RPM^3 - 8.2637$
FFV	$T = 3.7043E\text{-}05*RPM^2 - 0.7966$	$P = 2.1984E\text{-}07\ RPM^3 - 8.2350$
AWT MG	$T = 3.5419E\text{-}05*RPM^2 - 1.1726$	$P = 2.1527E\text{-}07*\ RPM^3 - 1.6279$
AWT	$T = 3.4340E\text{-}05*RPM^2 - 0.9620$	$P = 2.1495E\text{-}07*\ RPM^3 - 6.7337$

Table C.2. Equations of thrust and power in terms of tip speed for 14 mbar.

	Thrust (N)	Power (W)
FFH	$T = 2.2366E\text{-}07*\ RPM^2 - 3.4573E\text{-}02$	$P = 3.0398E\text{-}09*RPM^3 + 3.4061E\text{-}01$
FFV	$T = 2.2365E\text{-}07*\ RPM^2 - 3.3938E\text{-}02$	$P= 3.0459E\text{-}09*RPM^3 + 3.8430E\text{-}01$
AWT MG	$T = 2.1451E\text{-}07*\ RPM^2 - 3.5553E\text{-}02$	$P = 2.9254E\text{-}09*RPM^3 + 1.8887E\text{-}01$
AWT	$T = 2.0699E\text{-}07*\ RPM^2 - 2.8866E\text{-}02$	$P = 2.9032E\text{-}09*RPM^3 + 3.1993E\text{-}01$

Table C.3. Equations of thrust and power for FFH assessment in terms of tip speed at 20 mbar, 30 mbar, and 42 mbar.

FFH	Thrust (N)	Power (W)
20 mbar	$T = 3.1858E\text{-}07*RPM^2 - 4.8708E\text{-}02$	$P = 4.3394E\text{-}09*RPM^3 + 5.2473E\text{-}01$
30 mbar	$T = 4.9002E\text{-}07*RPM^2 - 6.4192E\text{-}02$	$P = 6.6935E\text{-}09*RPM^3 + 9.2267E\text{-}01$
42 mbar	$T = 6.8745E\text{-}07*RPM^2 - 1.0116E\text{-}01$	$P = 9.3878E\text{-}09*RPM^3 + 1.1438$